Turbulent Flame Speed of a Gasoline surrogate in conditions representative of modern downsized Spark-Ignition engine

M. Di Lorenzo, Pierre Brequigny, Fabrice Foucher, Christine Mounaïm-Rousselle

HAL Id: hal-03559599
https://hal.science/hal-03559599

Submitted on 7 Feb 2022

Turbulent Flame Speed of a Gasoline Surrogate in conditions representative of modern downsized Spark-Ignition Engine

M. Di Lorenzo, P. Brequigny, F. Foucher, C. Mounaim-Rousselle
Univ. Orléans, INSA-CVL, PRISME, EA 4229, F45072, Orléans, France
corresponding author : pierre.brequigny@univ-orleans.fr

Highlights

- Turbulent flame speed measurements of a gasoline surrogate in conditions similar to a downsized spark-ignition engine-like are presented using two different setups and different integral length scale

- Important variation in Dahmkohler and Karlovitz number were investigated to study several combustion regimes

- Several Turbulent flame speed correlations from the literature were tested

- A new turbulent flame speed correlation is proposed and validated on different datasets.

Abstract

The downsized spark ignition (SI) engine is considered as one promising technology to reduce pollutants and greenhouse gas emissions. By boosting the intake air pressure, this operating mode achieves higher efficiency, thus reducing pollutant emissions. Modelling the combustion process in these drastic conditions (high pressure, high temperature and high dilution rate) remains challenging, however, since most of models of premixed turbulent combustion seem insufficiently robust because the turbulent combustion regime might be out of the classical flamelet regime. Two different setups, a spherical vessel and a one-shot engine, were used to study turbulence-flame interaction in conditions representative of a modern downsized SI engine, i.e. under high pressure, high temperature and high dilution and controlled turbulence. Turbulent flame speed were measured in a wide range of Damkohler and Karlovitz number. Several turbulent flame speed correlations from the literature are also tested and compared to the complete experimental dataset gathered on both setups.

Keywords

Turbulent flame speed; spherical expanding flame; gasoline surrogate, dilution, turbulent flame speed correlation

Introduction

Premixed turbulent combustion remains a significant problem for practical combustion processes such as those found in stationary power gas turbines, spark-ignition (SI) engines, and explosions despite the increasing number of studies carried out over the last 60 years. The issue becomes particularly crucial with the use or future use of premixed turbulent combustion in increasingly drastic conditions in terms of pressure, temperature and diluted environment. One example is the modern downsized Spark-ignition (SI) engine, which can operate at higher pressure than conventional engine and therefore requires dilution to avoid knock and damage to the engine. Besides, the use of such conditions questions the validity of current CFD model used for the design of downsized engine.

The investigation of turbulent burning velocity, S_T, considered as the main parameter of turbulent premixed flames, motivated several studies in the recent decades. Nevertheless, the great part of these works were conducted at atmospheric pressure and room temperature conditions ([1–3]) and only recently researchers are focusing on experiments at higher thermodynamic conditions. More and more studies considered the effect of pressure, but mainly at room temperature ([4–8] among the others), as only a few high temperature ([9–12]). Among these, Jiang et al. [11] investigated expanding premixed methane/air flames for a temperature between 300 and 423 K and a pressure from 1 to 5 bar with a turbulent intensity, q', from 1.43 to 5.6 m/s. Despite this appreciable range of conditions, the integral length considered was relatively large, i.e. between 34.4 and 45 mm, without the investigation of dilution effect. Kobayashi et al. [10], on the contrary, focused on the effect of dilution up to 10% CO_2 dilution rate, using a methane/air Bunsen-type burner in a high-pressure chamber (5 and 10 bar) at 573 K. They associated the decrease of the turbulent burning velocity to the decrease in local burning velocity due to the flame stretch, through the Markstein length. Yet, they observed that CO_2 dilution reduces the wrinkling scale of the mixture CH_4/air, increasing the mean volume of the turbulent flame region demonstrating the possibility of restrict the combustion oscillation of premixed gas turbines.

Ahmed et al. [12] studied the 3D behavior using a scanning Mie-Scattering Tomography and compare their results with 2D flames. The maximum initial pressure was 5 bar but they were able to measure turbulent flame speeds at higher pressure under constant volume assumption. This study focuses on hydrogen and methane and provide results regarding the stretch factor with much higher values for hydrogen than methane. Their studies also concluded that the usual assumptions of isotropy used to rely on 2D flames results in spherically propagating kernels are not well supported: 3D displaying very different area ratios compared to 2D, and that might be due to a movement of flame kernels during propagation.

Only few studies are for liquid fuel [13–18]. Most of these studies used isooctane, like the one of Lawes et al. [15] focused on flame propagation in a turbulent vessel from 1 to 10 bar with q' from 0.5 to 6 m/s. In this study, quenching phenomena were observed at $\phi = 0.8$ and $q' > 2$ m/s. Moreover, the increase of q' led to a shift of the maximum equivalence ratio at which the S_T peak is observed. At low $q' = 1$ m/s, S_T was observed to remain constant while for $q' > 4$ m/s it increased slightly. Mannaa et al. [17] studied flame propagation with more realistic fuels, i.e. FACE-C gasoline and its surrogate, showing the competing effect of turbulence, pressure, and laminar burning velocity. Bradley et al. [18] characterized turbulent flame speed of premixed ethanol-air with pressure up to 12 MPa, which is still one of the highest pressure studied for that kind flame under constant pressure assumptions.

Scattering in results and observations, within the topic of the turbulent premixed flames, derives from the use of very different experimental set-ups in which the fundamental properties of the turbulence may strongly vary from one study to another. In addition to the case of spherically expanding flames, the Bunsen-type burner is one of the most used setup to investigate turbulent flames at high Karlovitz numbers. Only one work by Liu et al. [19] directly focused on the Karlovitz number effect on turbulent expanding flames. In this study, Karlovitz number ranges from 0.4 to 4.3, with a pressure increase up to 10 bar but a large integral length value between 23.2 and 45 mm. It was found that, to increase S_T, the intensification effect caused by an enhancement of the turbulent intensity is much more effective than the instabilities generated by pressure increase. But, more important, the work shows that the turbulent burning velocity decreases with increasing pressure in a minus exponential

manner similar to the unstretched laminar burning speed S_L, when Reynolds number is constant. But, if *Re* increases the turbulent burning velocity increases.

Studies carried out on Bunsen-type burner usually focus at higher ranges of Reynolds and Karlovitz numbers exploiting very high values of *q'* [3,20–22] with also the investigation of the limits of the different combustion regimes zones on the Peters-Borghi diagram. In this respect, recent works of Driscoll et al. [23] and Skiba et al. [20], redefined limits and definitions of the most important combustion regimes on the Peters-Borghi diagram, considering intense turbulence cases ($Re_T > 2800$ or $Ka > 100$) and concluded that some of the usual limits fail in prediction and unification of experiments and DNS available in literature. This implies that further investigation is necessary to conclude about the existence of a net boundary between the different combustion regimes.

One of the main difficulty is the comparison between results from different experimental set-ups, due to the great number of variables that play a role in the S_T determination. For this reason, most of the time the way is to find an universal correlation to predict the turbulent flames behavior from the knowledge of the most important fundamental parameters [24]. The investigation of classic correlations [24], [25] and the formulation of new ones, are still an open topic. Remarkable works, in this sense, are those of Chaudhuri et al. [7], Wu et al. [8] and Nguyen et al. [26], performed on spherically expanding flames. Wu et al. [8] observed the local quenching for lean mixture ($\phi = 0.8$) and high turbulent intensity ($q' = 5.24$ m/s), and proposed a new version of the correlation initially proposed by Chaudhuri et al. [7]. In more recent study, Nguyen et al. [26] tried to improve three recent correlations by adding the effect of the Lewis number. Last, Brequigny et al.[16] and Burke et al. [27] recently compared several correlations available in the literature in comparison with experimental data and showed the importance of taking into account the Lewis number into those correlations as for the correlation of Muppala et al. [28]. Brequigny et al. also showed the importance of having a well-identified definition for S_T to get a well-defined correlation for this parameter.

As the main idea of this paper is to observe flame propagation in different initial conditions and therefore combustion regime itself, as much representative as possible of modern downsized SI engine, the objectives of this paper are multiple:

- Studying a gasoline surrogate, i.e. TRF-E, designed to be very similar to a commercial gasoline [29], in turbulent conditions and then providing S_T measurements in a wide range of conditions of pressure, temperature and turbulence by using two different experimental setups: a well-known spherical vessel and the New-One Shot Engine described in the following sections.

- Using high dilution rate (until 25-30%) to reach unusual high Karlovitz numbers thus allowing to potentially change the combustion regime, at the boundary of flamelet regime limits where current CFD model could have a lack of precision as already suggested by Mounaïm-Rousselle et al. [30].

- Suggesting a new correlation for S_T as a function of characteristic parameters, valid for all combustion regimes covered by the present study but also compared with other literature data.

Experimental Setup

In this work, the premixed turbulent combustion of a gasoline surrogate, i.e. TRE [29] (44 % iso-octane, 36 % toluene, 15% n-heptane, 5% ethanol), is studied by means of two experimental setups:

- (i) the turbulent spherical vessel, fully described by Galmiche et al. [31] and already used for several premixed turbulent combustion studies [14,16,17,32–34],
- (ii) the NOSE (New One-Shot Engine) setup, initially designed for Spray-A study in ECN framework [35,36] but updated for premixed combustion studies.

Since the spherical vessel has been now extensively described, only experimental details about NOSE set-up will be covered in the following sections for the sake of conciseness.

NOSE set-up characteristics

The working principle of NOSE consists in using an ideally adiabatic compression process to accurately reproduce high temperature and pressure conditions. The core of the experimental set-up apparatus was firstly characterized and fully described in recent works [35–37]. A scheme of NOSE set-up is given in Figure 1.
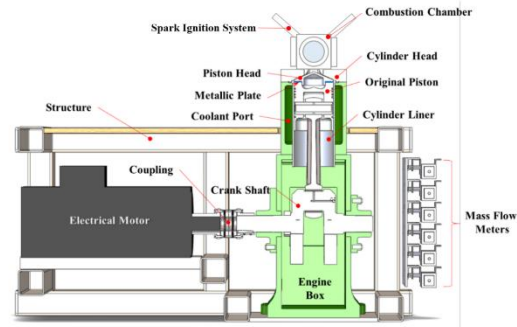
Figure 1. Scheme of the whole NOSE apparatus, adapted from [37]

The core of the set-up is a single-cylinder 18 horsepower diesel engine with an initial volume of 3600 cm^3, a bore diameter of 155 mm and a stroke of 177.8 mm. The initial and final volumes can be varied by adding a plate of a specific thickness between the head and the body of the piston. This allows providing different initial Compression Ratio (CR). By using an extended cylinder body, the CR can be drastically reduced. In the present study, two geometries will be considered: first one named 'Standard Volume' (SV), with a CR of 9.78 and second one, 'Large Volume" (LV), with a CR of 1.99. The cylinder head hosts the intake, the exhaust, the purge, the vacuum pump lines and the dedicated combustion chamber, as shown in Figure 2 (a).
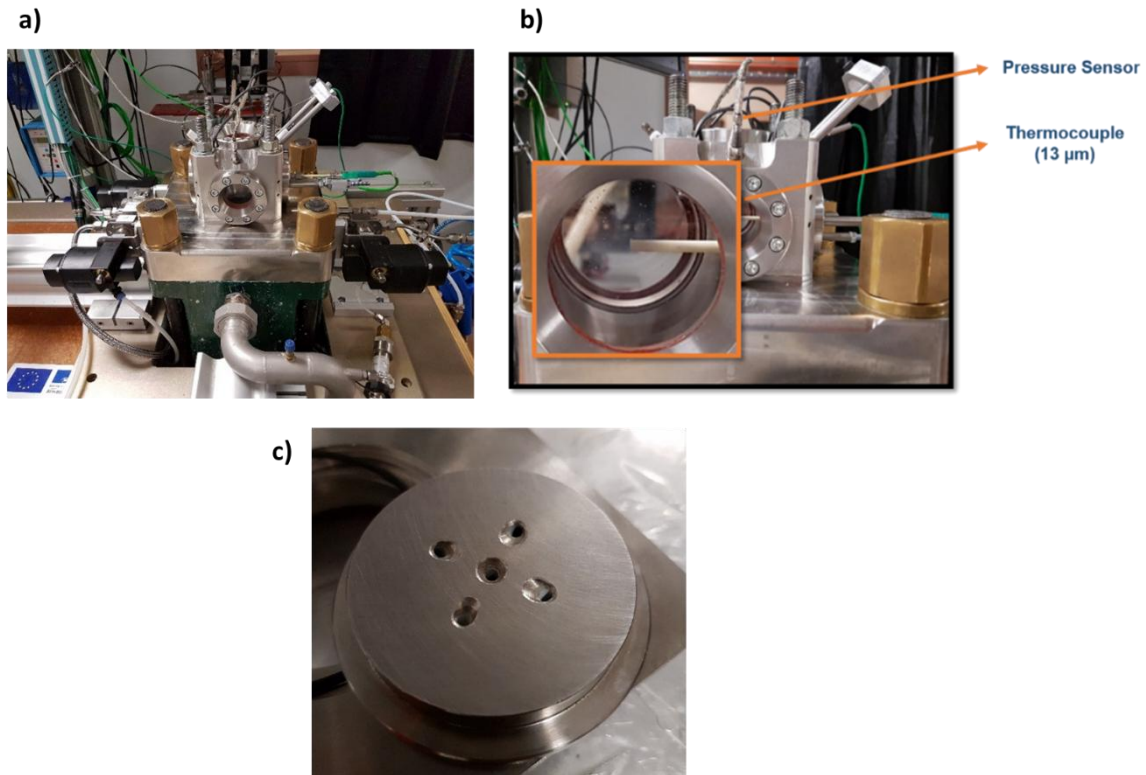
.

Figure 2. a) Combustion chamber views and details of the combustion chamber main sensors and b) pressure transducer and thermocouple; c) Details of flow generation grid.

The designed chamber set here is internally spherical shaped with a 40 mm radius, equipped with four cylindrical quartz windows of 18 mm radius. Four resistive heaters can be used to warm up the chamber. Two tungsten electrodes and an automotive ignition coil compose the spark ignition system. Between the combustion chamber and the cylinder head a smooth connection or a 'flow generation' grid can be added to modify the internal flow field of the compressed gaseous mixture inside the chamber itself. The grid shown in Figure 2 (c) is used to generate turbulence, numerically designed by using Converge CFD (during 'MACDIL' ANR-15-CE22-0014 project) and experimentally validated in [38]. It presents 5 holes, of which one centered and without inclination, and the 4 other holes inclined of 27° radially and externally directed with respect to the central axis.

First, the system is warmed up at the desired initial temperature, with a maximum initial temperature of 473 K for the combustion chamber and 373 K for the cylinder/piston system. Once the desired temperature is reached (according to the targeted one at the TDC), the piston is normally positioned at Botton Dead Center. A vacuum pump is used to extract all the gases before starting each test, until

reach a minimal pressure of 1 mbar. By setting the desired mixture molar fractions, a set of flow meters, as Bronkhorst mini CORI-FLOW (30 g/h) for liquid fuels or water or BROOKS® model 5860S gas flow meters for N_2, O_2, CO_2, or gaseous fuels is used to inject the correct volume of each component with a precision of $\pm$ 0.7%. Liquid components are carried on by the gas flow inside a heated capillary tube, allowing the vaporization. According to the composition of the burned gases in a stoichiometric air/TRF-E flame, the synthetic exhaust gas recirculation (EGR) composition is 13.62% CO_2, 12.22% H_2O and 74.16% N_2. After each test, gases are expulsed through the exhaust line and a purging line with dry air at 7 bar is opened to clean residuals. A piezo-electric low-pressure sensor KISTLER Type 7001 tracks pressure during the filling process. The maximum initial pressure is 10 bar, as the transducer limit. The pressure and the chamber gases temperature are tracked by a high-pressure sensor KISTLER Type PAA-33X/80794 and a 13 μm K-type thermocouple, as shown in Figure 2 (b), respectively, in non-reactive conditions to validate the temperature homogeneity and repeatability during experiments.

Pressure, temperature, crank angle degree, velocity feedback and electric motor response are recorded as a function of time through a National Instrument Compact RIO at 250 kHz. The ad-hoc configured Lab-View software allows the control of the system, by adjusting the piston velocity trajectories, monitoring the main parameters and phasing the trigger signals (spark timing, high-speed camera, etc.). Figure 3 shows pressure and temperature traces for different NOSE configurations, explained in the following. The squared zone indicates when the conditions are considered constant and therefore the period when ignition is allowed.
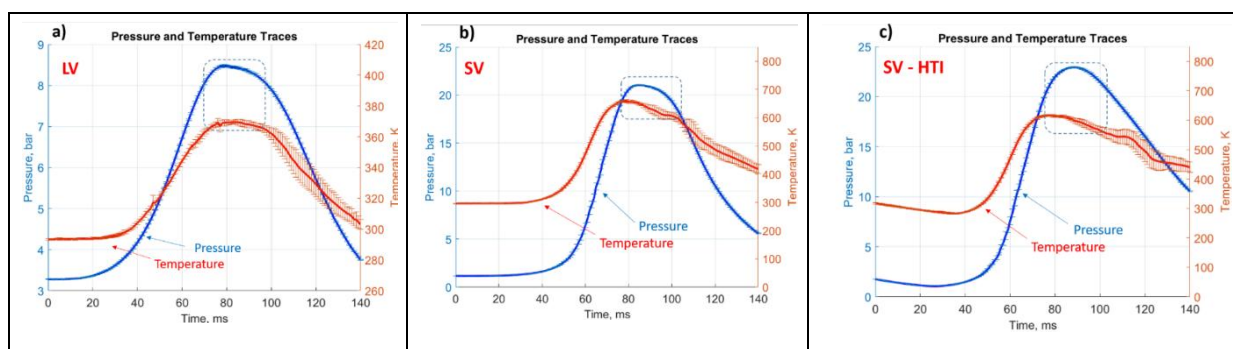

Figure 3.Repeatability for 10 individual tests for

a) Large Volume; b) Small Volume c) Small Volume with High Turbulent Intensity.

Three configurations for different targeted conditions.

In the present study, three configurations of NOSE were considered to generate different turbulent conditions:

1) based on LV configuration, low temperature and low pressure (LT-LP) condition

2) based on SV configuration, a high temperature and high pressure (HTHP) condition

3) based on SV configuration but with a particular piston movement trajectory to increase the turbulence, a high temperature - high pressure conditions with high turbulent intensity (SV-HTI). To modulate the turbulence intensity:

- either the piston starts at the BDC and runs one 'tour' before returning at the initial position

- or before starting, the piston is slowly moved backward at 80°CAD in order to take advantage of the initial non-zero velocity of the piston, to better counteract the system resistance with a stronger acceleration before sharply slowing down at the TDC. This new trajectory was designed to increase the turbulent kinetic energy (TKE) without changing CR and thus the *plateau* thermodynamic parameters.

Figure 3 highlights the level and the repeatability of pressure and temperature reach for 10 identical tests performed for these three configurations. The ignition of the mixture and therefore the flame observation are triggered when the pressure reaches a plateau (near TDC) delimited by dotted rectangle of Fig. 3 in order to be as much as possible under constant pressure condition.

The flow field of NOSE as a function of the configurations was deeply investigated in a previous work, by using PIV technique [38]. The fundamental turbulent parameters such as kinetics turbulent energy, isotropic ratio and different integral length scales were determined and compared with turbulent spherical vessel. Even if the homogeneity and quasi-isotropic hypothesis could be questioned, while stationarity may be assumed, the turbulent kinetics energy and the estimated turbulent integral length from [31](vessel) and [38](NOSE) as well as the laminar flame parameters obtained using the correlation proposed in [29] for TRF-E/air mixture are given to estimate Karlovitz

and Damkohler number in Table 1. Figure 4 shows the zones of the Peters-Borghi diagram covered by both setups. It has also to be noted that a wide range of *Da* values is obtained thanks to both set-ups ranging from nearly 1 to about 50. The range of Ka value from less than 1 up to almost 20 is very promising in order to reproduce combustion-turbulence interaction as in a boosted SI engine. Compared to the sphere, the NOSE setup enables to reach higher Reynolds level: below 1000 for the vessel and up to 2000 for NOSE due to higher turbulent intensity *q'*.

Table 1. Turbulent combustion properties for TRF-E/air mixture at $\Phi = 1$ and dilution 25% EGR for the sphere[31] and 3 NOSE configurations [38]

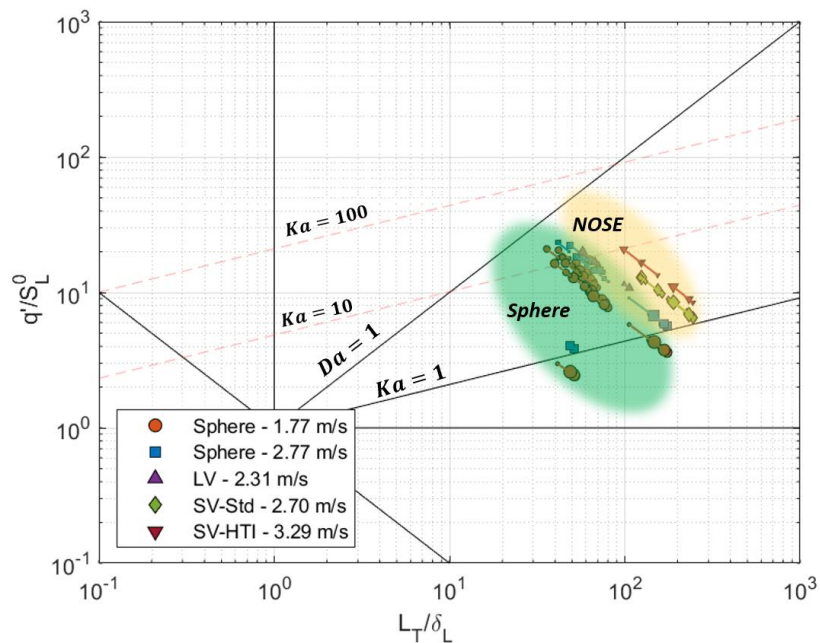|	q' (m/s)	L_T (mm)	S_L^0 (cm/s)	δ_L^0 (μm)	Ka	Da
Sphere [31] **– 473 K, 5 bar**	1.77 - 2.77	3.40	16.50	58.98	10.40	5.4-3.4
LV – 373 K, 8 bar	2.31	2.35	9.7	42.88	18.42	2.3
SV – 605 K, 21 bar	2.70	2.07	17.94	18.43	6.38	7.5
SV-HTI – 585 K, 21 bar	3.29	2.07	16.83	18.59	9.53	5.7

Figure 4. Peters-Borghi Diagram

Optical techniques on NOSE

The PIV setup previously used for aerodynamic characterization of NOSE and presented in [38] was replaced by Double-View Schlieren (DVS) to capture temporal flame evolution. DVS enables to simultaneously provide two different views of the flame propagation simultaneously recorded with one High Speed Phantom v1610 camera, to detect the possible irregularities and/or anisotropies in the 3D flame spherical shape, especially pertinent for turbulent flames. The DVS set-up is similar to the one already presented in previous works [16,29,32]. Images were captured with a resolution of 1280x800 pixel^2, by offering a spatial resolution of 0.0653 mm/pixel. The frame rate was adjusted between 5000 and 8000 fps depending on the propagation flame speed. From DVS technique, an estimate of the flame volume and its expansion as a function of the time can be done, especially useful for turbulent flames in which the equivalent radius based on the area may lack in consistency due to the 3D shape of the flame. Usually, it is done by means of an *ellipse method* [32]. The two side images (i.e., left and right as visible in Figure 7) are analyzed section by section, by taking each 1-pixel row and detecting a left and a right radius at each step. These two radii are the minor and major axis of the ellipse that better fit the contour of this section. The sum of all the ellipses represents the total volume of the flame. It is obvious this volume overestimates the 'real' one as the flame wrinkling is not taken into account. Yet the technique help in taking into account the 3D aspect of the flame even if it is not fully 3D as Ahmed et al. work.[12]. Moreover, as suggested by Bradley et al. [4,39], using Schlieren images implies that the detected contours already overestimate the real ones. Despite this, the volume overestimation normally does not significantly vary during the flame propagation, justifying the use of an equivalent radius based on the flame volume. For each condition a minimum of 6 tests and a maximum of 10 tests were performed, as a function of the recorded images quality. Therefore, for each experimental condition, the number of available radii is not the same for all tests, depending when the flame reaches the observation limits. Therefore, the average of the radius is done by considering the scattered data of all tests within a limited interval of radius (for the spherical vessel, between 5 and 15 mm, for NOSE between 4 and 12 mm) and a polynomial fit allows the interpolation of the missing

points. The fit is afterwards used for the speed calculation. The radius range is chosen in order to avoid ignition effect on the propagation. It was shown in [16] that for the sphere, the flame is no longer affected by ignition after 4 mm. In the case of NOSE, due to the higher of pressure and temperature, the minimum ignition energy allowed is lower than for the sphere. It was therefore possible to decrease the charge duration of the coil thus leading to a smaller minimum radius observation.

Results

The investigation of turbulent flames was carried out by means of the spherical vessel and the NOSE setup, for more than one hundred conditions, all detailed parameters are given in supplementary materials (SM) as SM1, SM2 and SM3. For each conditions, a minimum of 6 repeats were done in order to provide average values. In Figure 5, all conditions are displayed using a zoom on the Borghi-Peters diagram. For the sphere (orange and blue symbols), the widest range of equivalence ratio studied was 0.8-1.3. In Figure 5, the bigger the symbol is the higher is the equivalence ratio. Two initial pressures were tested: 1 and 5 bar. For this second pressure condition, 6 temperatures were investigated at q'=1.77 m/s: 343, 368, 390, 450, and 473 K and only 3 temperatures at q'=2.77m/s : 423,435 and 473K. Up to 4 dilution ratios were achieved: 0, 20, 25, and 30% at initial pressure of 5 bar for both q'. For NOSE, initial pressure and temperature as well as the turbulent properties are imposed by the configuration. For LV, pressure and temperature equal 8 bar and 373K, for SV-Std 21 bar and 605 K and for SV-HTI 21 bar and 585 K. 3 different dilution ratios were studied in NOSE: 10, 20 and 25%. The equivalence ratio range was reduced due to ignition issues and flame stabilization issues and covers stoichiometric to rich mixtures. Only one lean condition (ER=0.9) was possible in SV-Std configuration at 10% of dilution. The effect of all those changes in experimental conditions in Peters-Borghi diagram are represented as arrows in Figure 5 except for the equivalence ratio, which shows a non-monotonic behavior visible in the Karlovitz change. From leaner to stoichiometric mixture, the Karlovitz number decreases and from stoichiometric to rich conditions, it increases in Figure 5, since the size of symbols is proportional to the equivalence ratio. Variation of equivalence ratios in same condition of pressure, temperature, dilution and turbulent properties are connected in Figure 5. Besides, it has to be noted that some similar conditions for *Da* and *Re* can be reached in both

set-ups. Moreover, the flames in NOSE set-up will interact with smaller Kolmogorov eddies (around 5 µm in comparison to 15 µm in spherical set-up). It is necessary to remember that the Reynolds number used on the Peters-Borghi diagram is usually the one that refers to laminar flame, given by $Re_L = \frac{u'L_T}{s_L^0 \, \delta_L^0}$. Finally, the circle markers visible in Figure 5 indicate some experimental limits were the flame images can show some fragmentation leading to a wrong estimate of the flame speed. This will be discussed in the next section.
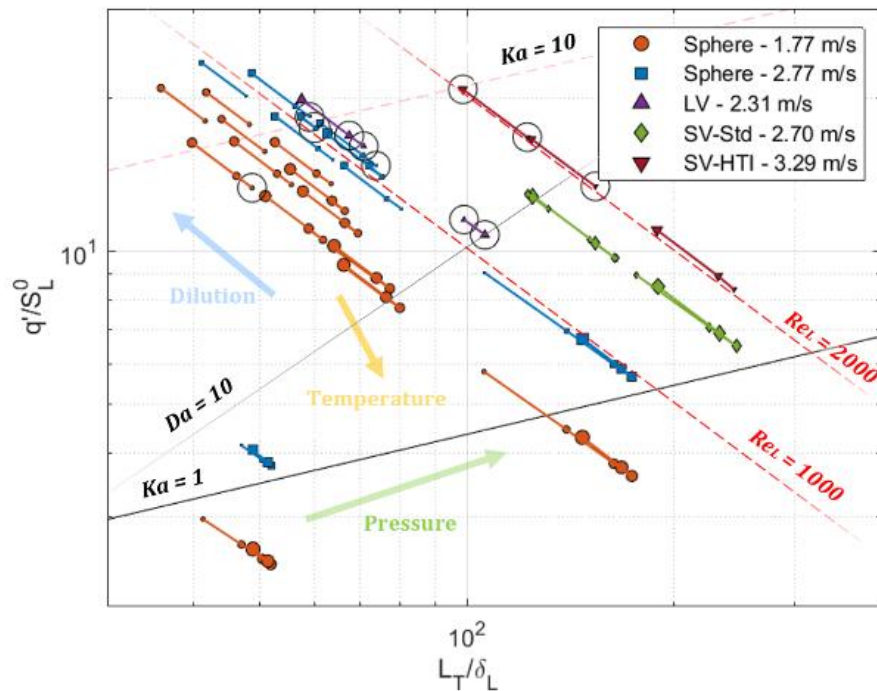

Figure 5. All investigated experimental conditions indicated in zoomed Peters-Borghi diagram. Size of symbol proportional to the equivalence ratio. Circle markers indicate the measured flame speed decreases during the expansion because of pockets formation and extinction.

Flame-turbulence interaction behaviour from images

Under certain conditions, the flame front may undergo local fragmentation yielding pockets formation. The appearance and the size of these structures seem to change with the turbulent flow properties. In the spherical vessel, the detected contour may be overestimated if these pockets stagnate on the flame surface. This phenomenon is likely to happen in particular for low turbulence and high dilution rates (above 25%). In these conditions, moreover, it was observed that flames might undergo to local

quenching. Similar quenching phenomena were observed by Wu et al. [8] for high q' (5.4 m/s) but ϕ = 0.8 and no diluent. An example of temporal flames evolution is given in Figure 6 , P = 5 bar, T = 423 K, EGR = 20%, $\phi = 1.1$ with a 2.77 m/s turbulent intensity. First, the flame shape is drastically affected by the largest turbulence eddies and during its propagation, the flame itself shifts and rotates. In the second image, this phenomenon causes a local thinning of a part of the flame that leads to a subsequent local fragmentation of the flame (more visible in the third image). The immediate consequence is a local quenching of the flame.

As pointed out by Bradley et al. [4] and recently discussed by Brequigny et al. [16], the Schlieren technique overestimates the radius R_v, defined such that the burnt gas volume outside the sphere of this radius is equal to the unburnt gas volume inside it, in comparison to the radius obtained from laser tomography technique. A correction factor has to be used to provide data independent to the measurement techniques. But due to the high ratio of q'/S_L^0 (see SM1, SM2 and SM3) and the non-perfect sphericity of most of flame shape, no correction has been used in the following data of raw radius R_S, defined as the radius determined from Schlieren images based on the burnt gas surface. Moreover, during some 'severe' conditions, the flames are strongly wrinkled and corrugated by the turbulence with a significant shift of the flame from the central position of the combustion chamber, as visible in Figure 7, leading to a reduced range of visualized radii. It has to be noted also that for some conditions, the circle markers of Figure 5, the temporal evolution of the radius is slowed down, indicated by the negative value of $\frac{d^2 R_S}{dt^2}$. As the temporal growth rate of the radius decreases, the turbulent flame propagation speed, V_T, will be also reduced as a function of the time. This could be due to the presence of local isolated fragments of some flame pockets into the fresh gases, certainly caused by the interaction between small scales of turbulence with the flame front under certain conditions.
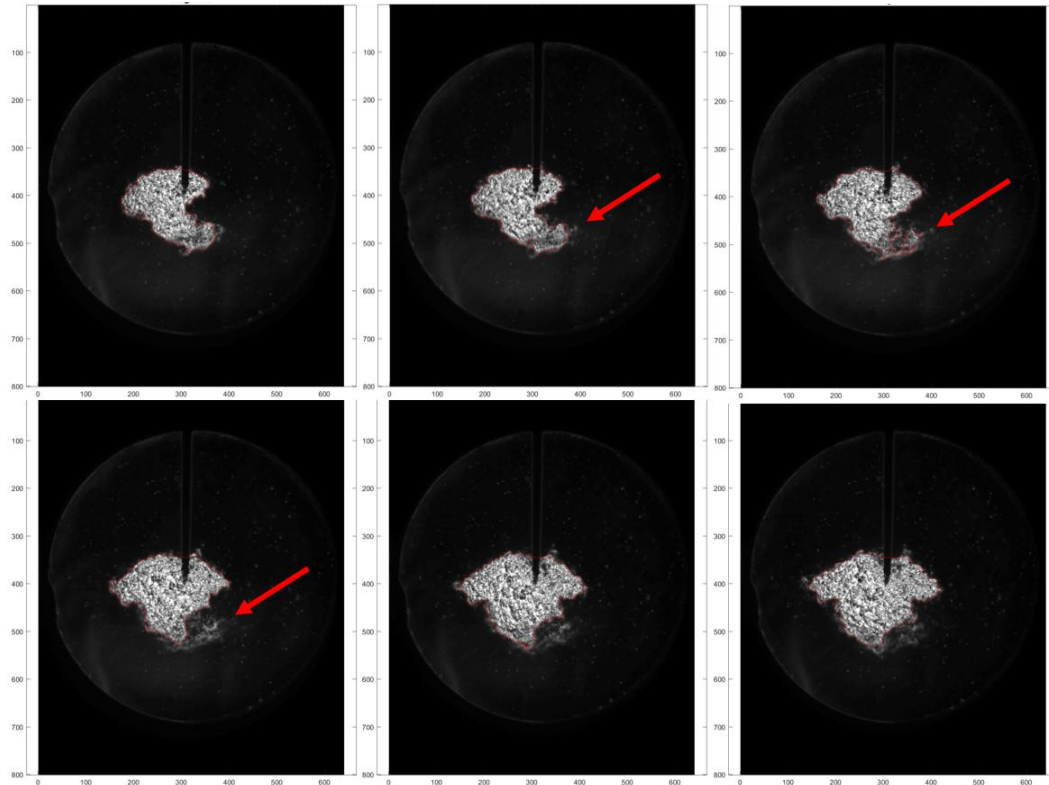
Figure 6. Examples of temporal flame evolution in spherical vessel (q' = 2.77 m/s, integral length 3.4 mm, P = 5 bar, T = 423 K, EGR = 20%, ER=1.1, Ka=7). Red arrows highlight local detachment and flame quenching. Time after spark: up= 3.2: 3.4; 3.8 ms, bottom= 4.2; 4.4; 4.8 ms(5000 fps).

In NOSE, similar phenomena are observed but the pockets are usually significantly smaller as it can be seen in Figure 7. Generally, the ensemble of these occurrences invalidates the flame speed measurements whose conditions seem to lie in a particular zone of the Peters-Borghi diagram and will result in a flame speed decrease observation as circled in Figure 5. As pointed out by Meneveau and Poinsot [40] some parametric limits for flames with partial or total quenching may correspond to the correlation $\frac{q'}{S_L^0} > 4\, Re_L^{0.25}$. Those specific cases will be referred as experimental limit cases and circled in the following figures.
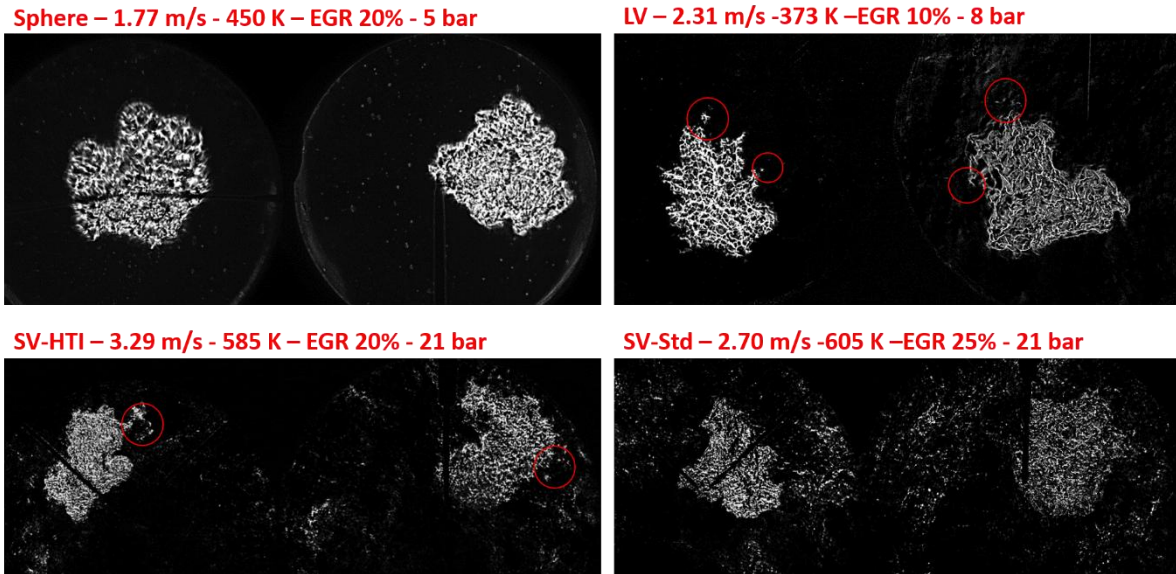
Figure 7. Flames examples for the low turbulent spherical vessel and the three NOSE configurations.

Flame propagation speed, wrinkling factor and flame barycenter displacement in spherical vessel

As reported in SM1 and SM4, tests performed on the spherical vessel were realized at 5 bar pressure, except for 2 reference cases (0% EGR, 1bar) and for two turbulent intensities, 1.77 and 2.77 m/s. It should be noted that the pressure increase affects less the *Ka* number than the temperature change. For this reason, to cover a large range of *Ka*, a range of temperatures, between 343 and 473 K was investigated for both turbulent intensities, to recover the full range of points achievable in NOSE. The main difference is that, with NOSE, the almost unexplored zone of Peters-Borghi diagram (as it can be seen in Figure 5) at very high values of q'/S_L^0 and L_T/δ_L^0 can be investigated. But the comparison for same value of Ka remains not so evident due to the difference also in integral length scale values between the two setups (3.4 mm for spherical vessel, while 2.07 mm for NOSE SV and 2.35 mm for NOSE LV).

Figure 8 shows the results of flame speed and barycenter shift in the vessel, for the reference cases at 1 bar and different *q'* (Figure 8 (a) and (b)), compared with an increase of pressure (from 1 to 5 bar, at 0% dilution, Figure 8 (c)) and an increase of dilution (from 0% to 20%, at 5 bar, Figure 8 (d)). It must be specified that the barycenter shift is an absolute value computed by considering the 3D

displacement, so by using the three coordinates obtained by the DVS technique. It can be seen that, for each graph of Figure 8, the barycenter shift ranking is inverse to flame speed ranking as function of the equivalence ratio. Indeed, if the propagation flame speed is not high enough to counteract the velocity field, the flame will be shifted before propagating itself. Hence, the lower the flame speed is the higher the barycenter shift. As the pressure increase (from Figure 8 (a) to (c)), the barycenter shifts tends to decrease at least for ER>0.8 in line with the flame speed increase from 1 to 5 bar. This beneficial effect of the pressure increase on the turbulent flame front is, probably due the promotion of hydrodynamic instabilities of the flame front as well as the decrease of the small turbulent scales (Taylor and Kolmogorov) encounter in the sphere as highlighted in [31]. The turbulent flame speed increases indeed from 2-2.5 m/s to 4 m/s.

For dilution (from Figure 8 (c) to (d)), since it will reduce the flame speed mainly because a laminar flame speed decrease, the barycenter shift will be more important. This trend is less evident when turbulent intensity increases (from Figure 8 (a) to (b)) where the increase of the barycenter shift is not as important as the flame speed increase but still noticeable.

More globally, the flame speed increase as function of the radius for all cases of Figure 8. The flame speed increases with the radius due to different reasons. The turbulent diffusion [41] can take part in the flame speed increase [42,43]. Driscoll [42] has reminded that the squared turbulent flame brush thickness δ_T^2 can be assumed proportional to the product of the turbulent diffusivity and time so that $\delta_T^2 = (q'L_T)^{0.5}.t^{0.5}$. As a consequence the turbulent flame brush will increase over time thus producing more flame wrinkling and then increasing the flame speed. Besides, the interaction between the flame front and the turbulence is not instantaneous. It will take time to the flame to be affected by the full spectrum of the turbulence as highlighted by Mannaa et al. [17] and leading to a continuous flame speed increase.
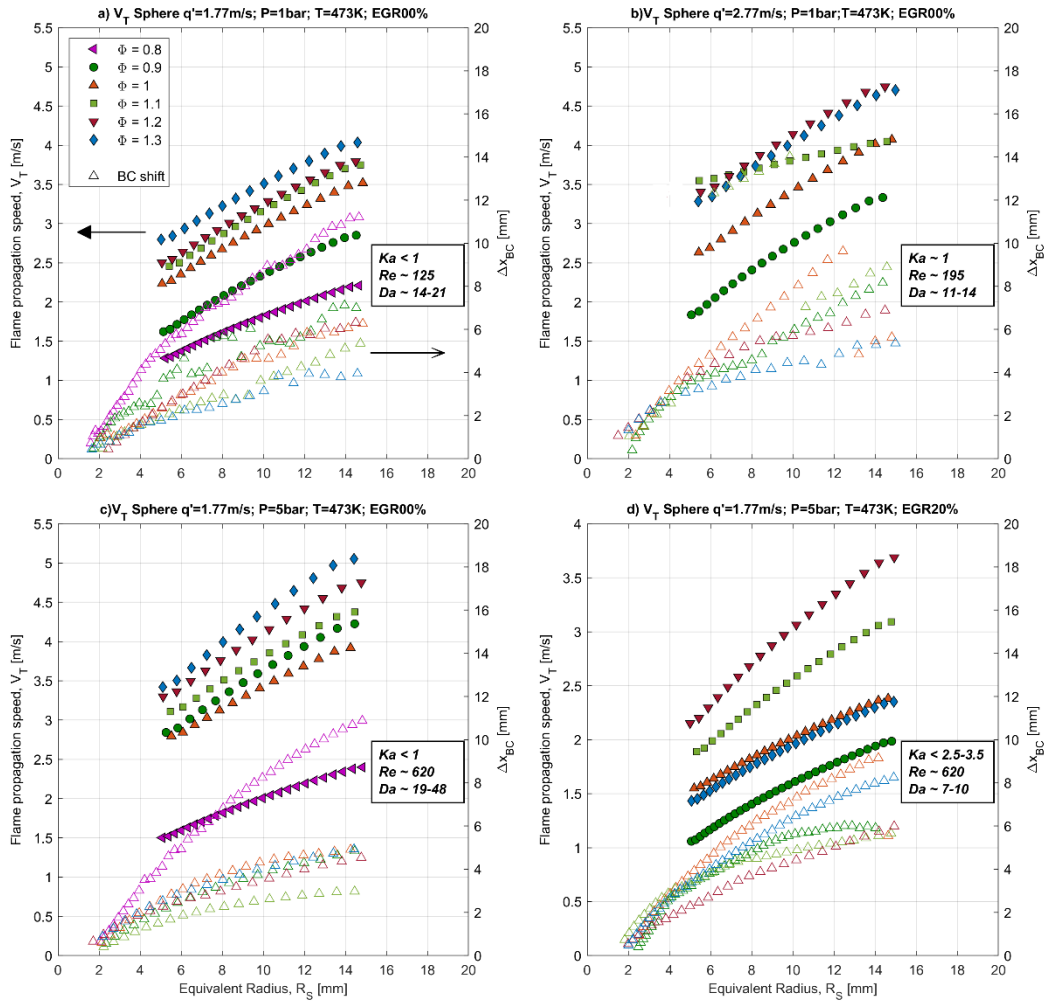
Figure 8. Turbulent flame propagation speed (left y axis), absolute barycenter displacement ('BC shift') in 3D domain (x, y, z directions) (right y axis) measured on spherical vessel for different experimental conditions.

In order to directly compare the characteristic turbulent flame propagation speed under all the different investigated condition, it is convenient to extrapolate a univocal value for each $V_T(R_S)$. In the present study, it was chosen to use $V_T(1.5T_T)$, the value of V_T, evaluated at the R_S at which the time is 1.5 the eddies turnover time for each condition of turbulence.

As highlighted in Figure 9, the evolution of $V_T(1.5\,T_T)$ as a function of ϕ is not classical 'bell' shape as it is for laminar flame speed evolution but increases continuously with the equivalence ratio. This increase, however, is stronger in the lean side than in the rich one, with a kind of plateau around $\phi = 1.1$ as can be seen in Figure 9. This trend was already observed in previous study of Lawes et al.

[15] and could involve the effect of the decreasing effective Lewis number, as pointed out by Han and Huh [44]. Normally, with such fuel, the increase of equivalence ratio causes a decrease of the effective Lewis number leading to more thermo-diffusive instabilities and wrinkling which should be responsible for a flame speed increase. Yet, at some moment, the wrinkles can recombine themselves leading to a decrease of the flame surface and a bending of the turbulent flame speed as already experienced experimentally in [34,45] and numerically in [46]. Figure 9 also highlight the effect of pressure on the flame speed with the data at 1 (blue squares and orange circles) and 5 (green diamond and purple triangle) bar being gathered separately. This pressure difference corresponds also to the Reynolds difference with a Re of 125 and 195 for the data at 1 bar while Re=620 for the data at 5 bar. It can be added that the data at 5 bar, u'=2.77, being the uppest on the graph also show the highest Karlovitz, i.e about 2.5-3.5 vs $Ka \leq 1$ for the three others datasets.
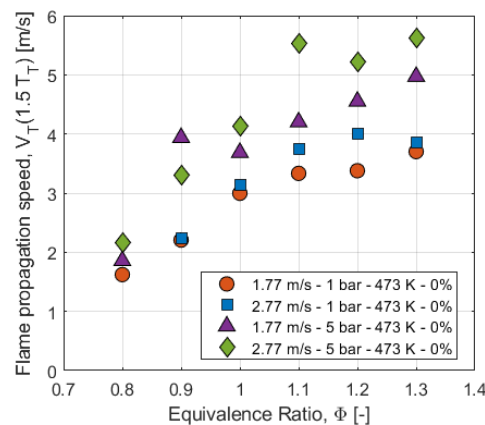

Figure 9. Effect of turbulent intensity and pressure on flame propagation speed, V_T $(1.5\ T_T)$.

In Figure 10, the effect of the dilution rate is evaluated for an initial pressure of 5 bar with turbulent intensity of 1.77 and 2.77 m/s. The increase of the dilution rate induces the decrease of the flame speed (Figure 8 from (a) to (b) repectively), so as the Ka number increases, as already highlighted in Figure 5. This flame speed decrease is probably due to a decrease of the flame wrinkles. As pointed out by Wang et al. [47], by considering the flame surface wrinkling as a key factor in the flame propagation speed, Reynolds and Karlovitz numbers have a direct influence. Indeed, the increase in Re increases the scales spectrum that will increase the flame surface area through its wrinkling. On the contrary, Ka

increase reduces the flame wrinkling and then causes the reduction of the flame turbulent propagation speed, even if this effect is weaker than the impact of *Re*. It has to be noticed that, for all considered experimental conditions, the Reynolds number, at one given temperature for fixed *q'* and L_T, is almost constant for all dilution rates and equivalence ratio. As a result, the effect of *Ka*, is clearly highlighted in Figure 10 through dilution since several *Ka* values are obtained (for several dilution rates) at constant *Re* number. On the contrary, the Reynolds number obviously depends on the turbulent intensity and on the pressure due to its impact on both S_L^0 and δ_L^0. As expected, the increase of *Re* contributes to the increase of the turbulent flame propagation speed in Figure 10 from q'=1.77 m/s;450K to q'=2.77 m/s ;473 K. For this reason, all the plots following will gathered conditions of similar *Ka* range.
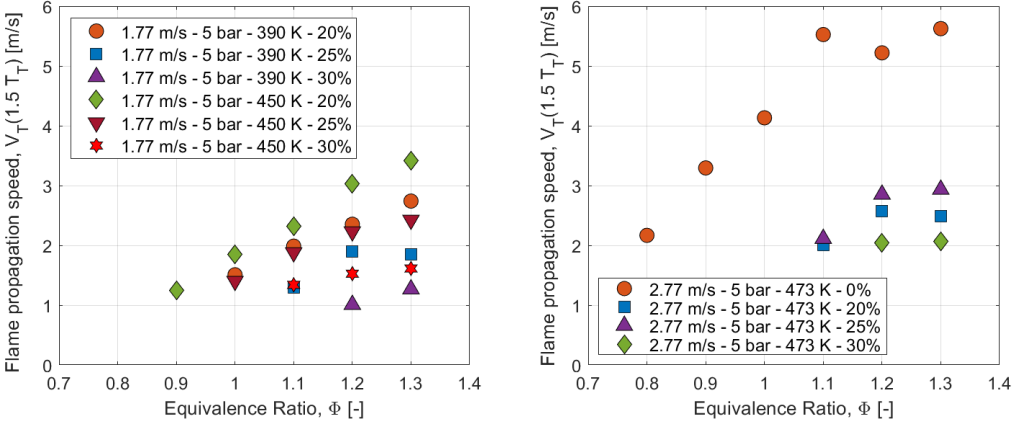

Figure 10. Effect of dilution on flame propagation speed V_T (1.5 T_T) for both turbulent intensities.

Figure 11 shows the evolution of turbulent propagation flame speeds, $V_T(1.5\, T_T)$ as a function of the equivalence ratio for different conditions (as temperature, turbulent intensity) but similar Ka range between 5 and 10. One clearly identifies here the boosting effect, over the whole range of the equivalence ratio due to the higher *Re* value (increase of about 200 for blue and black symbols), reached in higher turbulence conditions. One can see that the effect of temperature variation seems to be already taken into account once flames with similar Karlovitz number are compared as visible for the yellow diamonds and circles. This is confirmed, on the Peters-Borghi diagram Figure 5, where the variation in temperature is in the same direction as *Ka* variations.
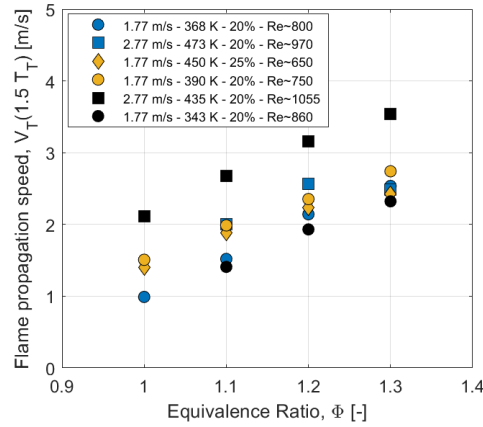
Figure 11. Effect of Re on flame propagation speed (at 1.5 T_T) as a function of the equivalence ratio for different conditions regrouped for same Ka range (blue: 4<Ka<6, yellow: 5<Ka<7, black: 6<Ka<9), P_{ini}=5 bar.

Figure 12 (a) reports the evolution of $V_T(1.5\,T_T)$ as a function of ϕ, for the lowest turbulent configuration ($q' = 1.77$ m/s), and the highest turbulent one ($q' = 2.77$ m/s) but for wider Ka ranges (7 to 12) and different Re values. There again, the impact of Re is clearly underlined: $Re \sim 750$ case (orange circles) induces $V_T(1.5\,T_T)$ trends slightly higher than the $Re \sim 650$ case (blue squares), almost coincident with the $Re \sim 800$ (purple triangle up) (that shows, anyway, higher Ka about 9-12 vs. 7-10 for both other Re cases). It has to be noted that for $q' = 1.77$ m/s, a kind of stabilization of $V_T(1.5\,T_T)$ value is reached. In fact, as observed in previous work by Lawes et al. [15], the monotonic increase of $V_T(1.5\,T_T)$ with the equivalence ratio starts to be dominant at moderate turbulent intensity ($q'\sim 2$ m/s). Finally, Figure 12 (b) reports data for the highest Ka range (>10), usually reached for low temperature and/or high dilution level (>25%). Under these drastic conditions, it is easy to observe the limits of the estimate of V_T, as previously discussed with the flame visualization and highlighted in Figure 7 where the detection displays an overestimation of the surface and leads to the limit cases previous circled in the Peters-Borghi diagram in Figure 5.
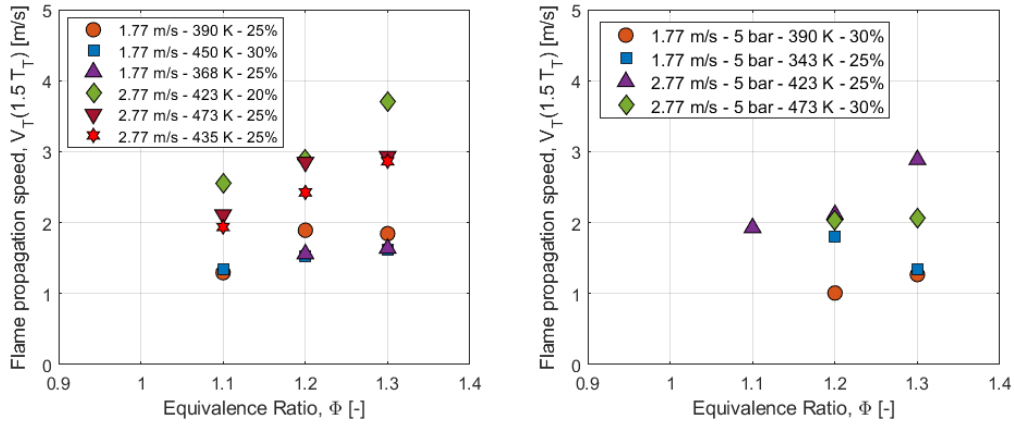
Figure 12. Evolution of flame propagation speed, $V_T(1.5\,T_T)$ vs. equivalence ratio for a) mid (7-10) and b) high (10-18) Karlovitz range, P_{ini}=5 bar.

Flame propagation speed in NOSE set-up

Experiments conducted on NOSE exhibit Karlovitz numbers in the same order of magnitude than those obtained on the spherical vessel, but with significantly higher Reynolds numbers for NOSE-SV conditions. Nevertheless, to compare the data obtained in NOSE and try to corroborate it with those obtained in our reference setup, i.e. the spherical vessel, the LV configuration allows similar pressure and temperature conditions with slightly lower turbulent intensity (2.31 m/s versus 2.77 m/s).

Figure 13 (a) reports the evolution of $V_T(1.5\,T_T)$ as function of ϕ to compare the results in the spherical vessel and in NOSE for similar Ka range, i.e between 2 and 4. Despite the higher *Re* in NOSE than in spherical vessel (between 1000 and 2000 for NOSE vs. 600 for the sphere), any significant effect on flame propagation can be noted. On the contrary, $V_T(1.5\,T_T)$ for NOSE SV-Std (EGR 20%), with *Re* ~ 1600, is lower than the tests performed on the spherical vessel at lower *Re*. Moreover, with the ϕ increase, the flame propagation speed increase is less pronounced, leading to a difference of about 40% at ϕ = 1.3. The points relative to NOSE SV-HTI, characterized by *Re* ~ 2060, follows same trends than data in spherical vessel. By considering the lower Reynolds numbers in spherical vessel (~ 620-650), it seems that when the pressure drastically increases the dependence on Reynolds number for $V_T(1.5\,T_T)$, previously observed on the spherical vessel cases, cannot be observed. By looking at

Figure 13 (b), the evolutions at same pressure (21 bar) with 10% EGR for $q' = 2.7$ and $q' = 3.29 \, m/s$, seem similar highlighting the balancing effect between Re, from 1600 to 2060, and Ka, from 2-3 to 3-4.
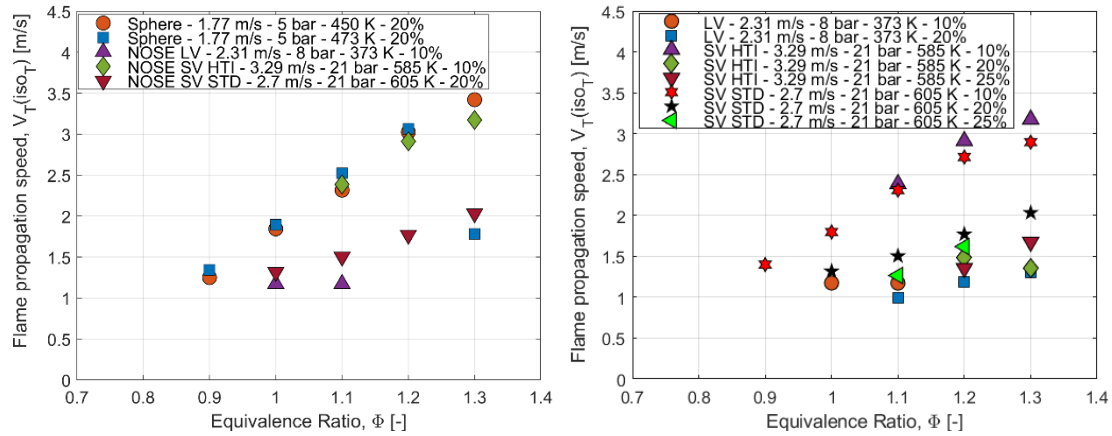

Figure 13. Evolution of turbulent flame propagation speed, $V_T (1.5 \, T_T)$ as a function of the equivalence ratio in a) sphere vs NOSE and b) NOSE only.

The main difference between experiments in NOSE and the spherical vessel is the high level of pressure reached. The effect of pressure increase on the turbulent flame propagation is the reduction of the chemical reactions characteristic time, represented by the Damköhler number, as it is the ratio between the integral turbulence temporal scale with this chemical time. The evolution of $V_T (1.5 \, T_T)$ for SV-Std is linked to the effect of integral length scale on the propagation velocity and its different value (2.07 mm on SV Std in comparison to 3.4 mm on spherical vessel). It was pointed out by Wang et al. [47] that small Kolmogorov scales can actually decrease the flame surface increase, partially counteracting the wrinkling enhancement due to the turbulent intensity, in the case of q'/S_L^0 up to 10. In their work, when the Kolmogorv scale was less than 20% of the flame thickness, the turbulent burning velocity reached a plateau. As shown in SM3, q'/S_L^0 is about 8,10 and 12 for the 10, 20 and 25% dilution for the NOSE SV-Std configuration. Another explanation not visible here, due to the Schlieren technique, could be the increase of the flame brush thickness. Indeed, the Kolmogorov scale for SV-Std configuration was estimated to 6.5 µm in [38] whereas the flame thickness (as visible in SM3) is about 8-10 µm for 10% EGR and greater than 12.6 µm for higher dilution. Hence, for 20 and

25% dilution, the small length scales are smaller than the flame thickness thus entering the flame front and leading to torn flames as in Figure 7.

Testing Classical Correlation for Turbulent Flame Speed

In the present section, correlations from the literature, to express the turbulent velocity as a function of initial characteristics parameters, are considered to evaluate the best one to represent turbulent flame propagation for the conditions of this study. As below, the turbulent propagation velocity value, $V_T(1.5\,T_T)$ is considered and multiplied by the expansion factor, $\frac{\rho_b}{\rho_u}$, to represent S_T in order to be consistent with the correlations based on the ratio $\frac{S_T}{S_L}$, as in the most usual one of Zimont [24]:

$$\frac{S_T}{S_L} = 1 + C\left(\frac{q'}{S_L}\right)^n \tag{1}$$

With C a constant. Figure 14 shows the evolution of all experimental values of $\frac{V_T(1.5\,T_T)}{S_L}\frac{\rho_b}{\rho_u}$ as a function of $\frac{q'}{S_L}$ for three equivalence ratios (1.1, 1.2, 1.3). Each symbol represents a temperature condition and different colors refer to the set-up configuration. The size of the symbol increases with the decrease of the dilution rate. A global agreement can be observed especially for the flames obtained in the sphere vessel but all data obtained for flames in NOSE are above, this is accentuated with the equivalence ratio increase.
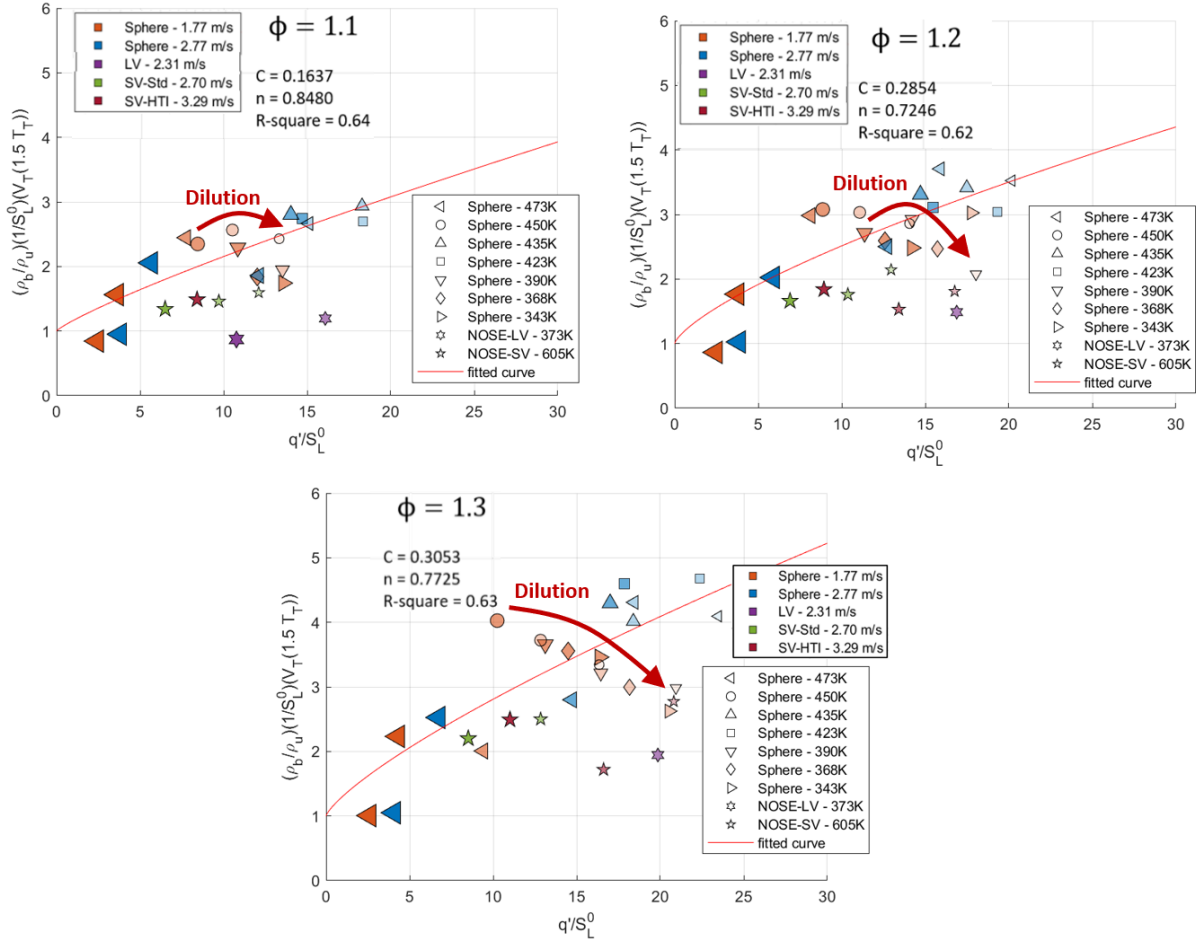
Figure 14. Validity of $\frac{S_T}{S_L} = 1 + C\left(\frac{q'}{S_L}\right)^n$ correlation with all experimental values of $V_T(1.5\,T_t)$ as S_T. Size of

symbol inversely proportional to the dilution rate

Following Nguyen et al. [26], three other correlations are tested. The first one is from Kobayashi et al.

[9,10], obtained for methane/air ($Le \sim 1$) jet flames as:

$$\frac{S_T}{S_L} \propto \left[\left(\frac{q'}{S_L}\right)\left(\frac{p}{p_0}\right)\right]^{0.38} \tag{2}$$

The second one was proposed by Chaudhuri et al. [7], for statistically spherical turbulent flames with

Le~1 based on a wide dataset of hydrogen, ethylene, n-butane, dimethylether, methane and isooctane:

$$\frac{S_T}{S_L} \propto \left[\left(\frac{q'}{S_L}\right)\left(\frac{<\bar{R}>}{\delta_L^0}\right)\right]^{0.5} \tag{3}$$

As third correlation, Liu et al. [6] introduced one to take into account the Damköhler number:

$$\frac{S_T}{q'} \propto Da^{0.5} \qquad (4)$$

Figure 15 reports these three correlations for the three equivalence ratios (from 1.1 to 1.3), with similar symbols as in Figure 14 but the equivalence ratio change is represented by the size of the symbol and the more transparent the symbol is, the higher the dilution rate. Nguyen et al. [26] pointed out the importance of including the Lewis number if tests are performed under high-pressure values (1-5 atm in their study), confirmed for Lewis number variation from 0.58 to 1.43. In this work, the Lewis number of the surrogate fuel based on three components was not computed due to the complexity of assessing the Lewis number of such blend. For sake of completeness, preliminary considerations have been done by using Lewis number of iso-octane as the major component of the surrogate. However, contrary to the results of Nguyen et al. [26], this approach did not produce significant improvement of the correlations.
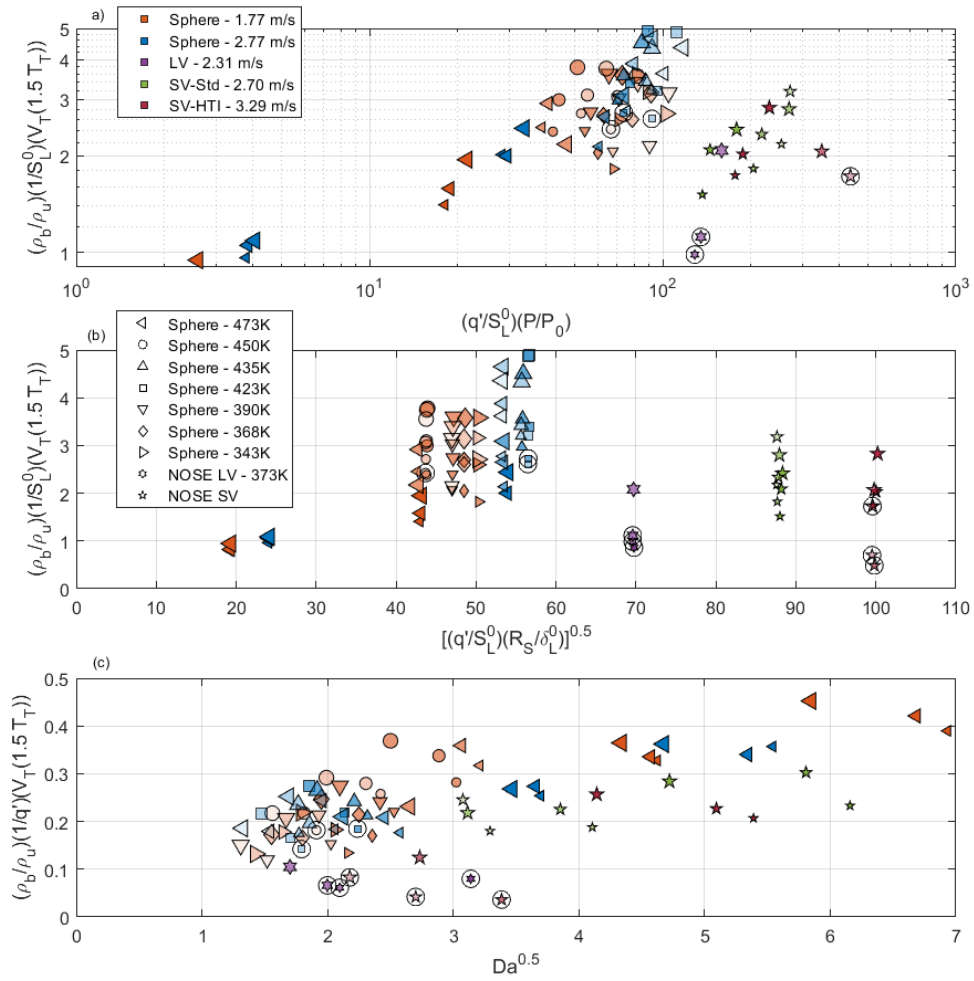
Figure 15. Evaluation of correlations to predict turbulence effect on flame propagation speed. Size of the symbol proportional to the equivalence ratio (1.1, 1.2, 1.3). Level of symbol transparencies is proportion to dilution rate. Circle correspond to the experimental limit cases. a) correlation Kobayashi (Eq.2) b) correlation Chaudhuri (Eq. 3) c) correlation Liu (Eq. 4)

In Figure 15 (a), the data obtained in spherical vessel are in partially good agreement with the correlation of Kobayashi et al. (Eq. (2)), except for minor scattering due to temperature and dilution variations. Yet, the correlation fails in the prediction of NOSE points, even for lower pressure (NOSE-LV) at 10% dilution rate. The fact that all NOSE experimental data are in the same zone may suggest an effect of the integral length scale on the resulting turbulent burning velocity, not considered in the present correlation. In Figure 15 (b), the vertical alignment of some experimental data is mainly due to

the dilution rate and the equivalence ratio increase. The effect of turbulent intensity and pressure increase is more evident for the data obtained in the spherical vessel. Data obtained in NOSE are not in the same predictive location. To deeply investigate this behavior, enlarged version of the correlation (Eq. (3)) as suggested in [8] is evaluated in Figure 16. All extrapolated radii are plotted against the relative $V_T(R_S)$, instead of using averaged R_S and extrapolated value of V_T. In Figure 16 (a), the effect of pressure, turbulent intensity and equivalence ratio increase is highlighted only for spherical vessel data, different symbols correspond to different equivalence ratio.
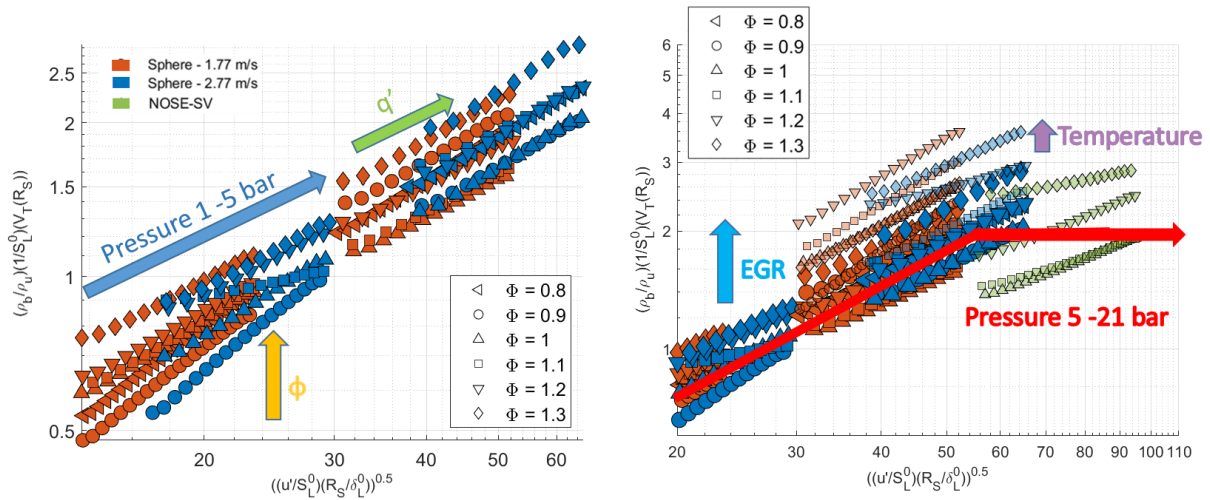

Figure 16. Evaluation of correlation proposed by Chaudhuri et al. [48] considering all the extrapolated radii and relative $V_T(R_S)$. a) spherical vessel configuration b) both configurations.

By adding the experimental conditions obtained in NOSE in Figure 16 (b), one can observe minor effects of temperature and dilution, but as a function of the pressure, the NOSE points are located in the right zone but not at the expected level. They are on the same level than spherical vessel data obtained at 2.77 m/s q' and 0% EGR. This drop may be related to the integral length reduction but also to pressure dependence quadratic law, similar to what was observed on the Peters-Borghi diagram and discussed previously. In a recent numerical study, Wang et al. [47] observed a plateau in the S_T trend for $\frac{q'}{S_L} > 8$ at fixed integral length. Nevertheless, when $\frac{q'}{S_L}$ was fixed and the integral length doubled, the S_T increased by more than 50%. The explanation of these results is that when q' increases two opposite phenomena balance the effect on the resulting S_T. The first is the broadening of the spectrum

of turbulent eddies that increases flame surface area. The second is the reduction of Kolmogorov scale that leads to smaller small-scales eddies that can affect the flame surface resulting in the loss of surface area through strain and curvature effects. On the contrary, when the integral length is doubled, the two phenomena act in the same sense, with both the broadening of eddies spectrum and the decrease of small-scale weakening effect. The last correlation of Liu et al. (Eq. 4), in Figure 15 (c), seems to better unify the experimental conditions of the different configurations and set-ups, evidencing the strong effect of the Damköhler number in turbulent burning velocity.

By exploiting the observed dependence of the turbulent burning velocity on Karlovitz number, the correlation proposed by Lawes et al. [15] based on the dataset of Bradley et al. [2] can also be tested:

$$\frac{S_T}{S_L} = A_b \frac{q'}{S_L} (KaLe)^{-0.3} \tag{5}$$

With $A_b = 0.88$. The Figure 17 reports this correlation with the current dataset. The correlation of Lawes, seems to show partial agreement at least with the data from the sphere and undiluted mixtures. Increasing dilution seems to increase the scatter in the data. When considering only the spherical vessel data the correlation gives an *R-square* of 0.55. Moreover, the correlation seems to be not able to follow the change in the experimental setup from the sphere to NOSE, i.e. the change in the integral length scales. Indeed, two clouds of data can be identified: one for the spherical vessel and one for NOSE setup. The linear fit of all data displayed in Figure 17 gives an *R-square* of 0.27 thus showing the poor agreement. Moreover, the slope obtained is 0.42 instead of 1 which leads to the correction of A_b coefficient down to about 0.47 which is between the value found by Brequigny et al. [16] (0.36) on the present spherical vessel with his dataset and the original value of Lawes et al. of 0.88.
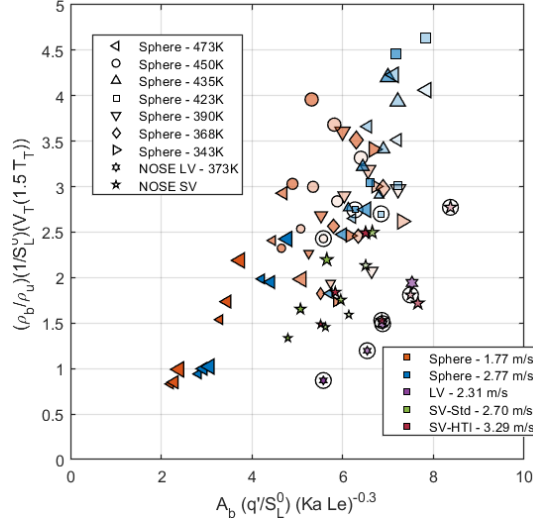
Figure 17. Evaluation of Lawes' correlation (Eq. 5) to predict turbulence and Lewis effect on flame propagation speed. Size of the symbol proportional to the equivalence ratio (1.1, 1.2, 1.3). Level of symbol transparencies is proportion to dilution rate. Circle correspond to the experimental limit cases

At this point, it seems that all the correlation tested fails in representing the whole dataset. Either they cannot catch both setups (eq. 2 and 3) or they fail when dilution is at stake (eq. 1 and 5). The best agreement, still partial, is found with Eq. 4 including Damköhler number. To fully account for the turbulence-flame interactions and the combustion regimes encounter in this study, and considering theis partial agreement observed for correlation including Da (Eq. 4, Figure 15 (c)) and Ka (Eq. 5, Figure 17) one may suggest a proportional relationship between S_T/S_L and $DaKa$ that yields the plots in Figure 18, with a fit equation as following:

$$\left(\frac{V_T(1.5\,T_T)}{S_L} \frac{\rho_b}{\rho_u} \right) = aDa(Ka)^b \tag{6}$$

For the gathered experimental database, *a* is 0.062 and *b* is 1.233, with an *R-square* of 0.90.
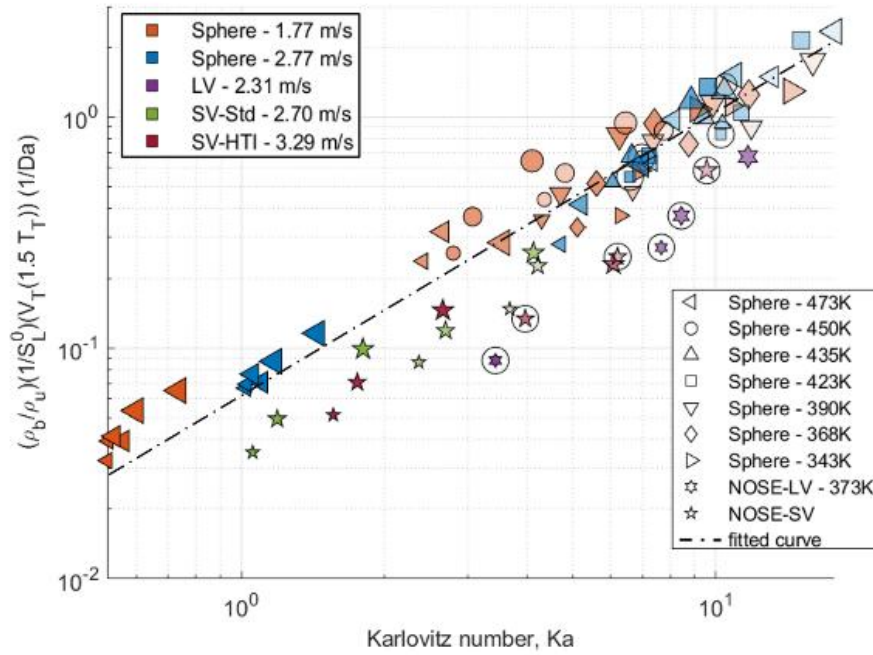
Figure 18. Correlation proposed in Eq. (6) for all the experimental conditions. Circle correspond to the experimental limit cases

With respect to the correlations available in the current literature, and briefly summarized in this work, the proposed fit equation seems to better represent the ensemble of the experimental points. It can be added that this correlation shows also good agreement for neat ammonia and ammonia/hydrogen blends in the sphere as shown in [34]. Especially the Karlovitz exponent is similar for both study 1.22 vs. 1.17 for Lhuillier et al. [34]. Wang et al. [49] also proposed recently a similar correlation based on Ka and Da but with exponents equal to 1 for *Ka* and 0.89 for *Da*, validated for methane, methane/ammonia, methane/ammonia/hydrogen blends and ammonia in oxy-combustion. Remembering the lack of accuracy of the experimental points circled in Figure 18, all the other points follow the proposed equation, function of just *Da* and *Ka*. Despite this, a minor dispersion is observed for low values of Ka and, in general, NOSE points tend to be slightly underestimated. To further improved the proposed correlation, experimental results obtained by Lawes et al. [15] for isooctane/air flames for a wide range of conditions (*q'* : 0.5, 1, 2, 4, 6 m/s, initial pressure : 0.1, 0.5, 1.0 MPa and equivalence ratio : 0.8, 1.0, 1.2, 1.4), at a 360 K initial temperature are included. Moreover, the integral length, that may represent one of the key parameters, is 20 mm, larger than the ones of the present study, being 2 to 3.5 mm. This can also allow understanding if the underestimation

of the NOSE experimental points may depend on the integral length. On the other hand, it must be underlined that the criteria for the extrapolation of the flame propagation speed were different: the value of the flame propagation speed was considered at $R_S = 30\ mm$, named $u_T(30)$. Despite all, as reported in Figure 19, all data from Lawes et al. as well as from the present study, are appreciably well described by the proposed fitting law with *a* and at *b* optimized values at 0.040 and 1.559 respectively, to provide a *R-square* of 0.99. It can be noted that the Karlovitz exponent increases when considering the data of Lawes et al. compared to the Figure 18 and the previous work of Lhuillier et al. [34]. Last, two DNS studies [50,51] were compared to the present experimental data and the ones of Lawes et al.. Both study shows similar trends with Karlovitz dependence in agreement with the experimental data and the fits with slopes that seems to agree better with the fit based only on the present data. For the DNS data of Aspden et al. [50], they show a Karlovitz exponent of 1.17 (vs. 1.223 for the present dataset) without considering the last point, which shows some bending compared to the three others. Those DNS were carried out in very similar conditions as the present study with lean methane, $\phi = 0.7; S_L^0 = 18{,}9\ cm.s^{-1}; L_T = 2.6\ mm$ and *q'* ranging from 0.3 to 2.3 m.s^{-1}. It can be noted that the laminar flame speed is low and therefore similar to diluted mixture of the present paper or to low burning fuel such as ammonia [34]. For the DNS data of Nivarti and Cant, they display a Karlovitz exponent of about 0.83 which is lower than what is observed here or in other experimental studies [15,34,52]. It should be reminded that those simulations were carried out with a higher laminar flame speed ($S_L^0 = 39\ cm.s^{-1}$) with very high Karlovitz values (between 12 and 100). Last, the major differences between the DNS and the experimental data is the turbulence evolution. Indeed for DNS the turbulence is decaying during the simulation whereas for experiments, the turbulence is either sustained by the fans (Sphere and Lawes et al. [15]) or affected by the piston motion in the case of NOSE.
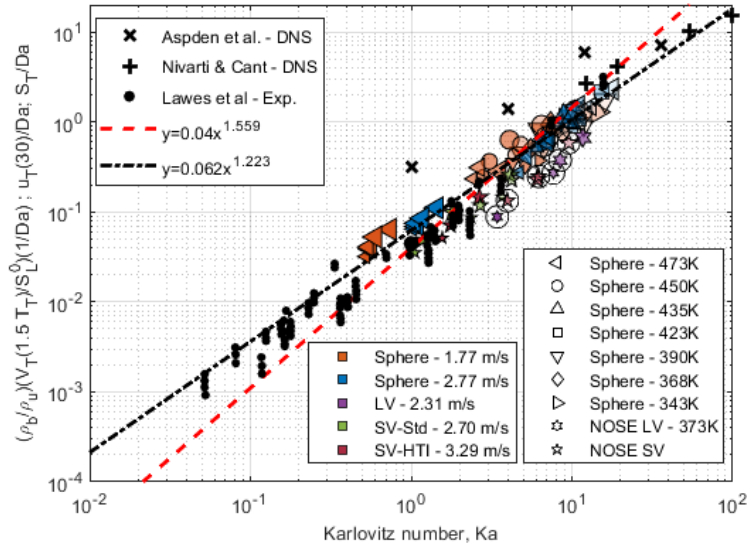
Figure 19. Correlation proposed in Eq. (6) for Lawes et al. data [2,15] (symbols on right) and all experimental data for sphere and NOSE. Comparisons with DNS studies of Aspden et al. [50] and Nivarti and Cant [51]. Black dotted line, initial fit from Fig. 18. Red dotted line, optimized fit with Data from Lawes et al. Circled points correspond to the experimental limit cases.

CONCLUSIONS

The major part of experiments performed on the spherical vessel were performed at 5 bar and covered a wide range of Karlovitz numbers, by varying temperatures, turbulent intensity and dilution. Reference tests at 1 bar, 473 K and 0% dilution were used as a direct comparison to observe the effect of increasing dilution and pressure (between 1 and 5 bar). Large increase of dilution rates, from 20% to 30%, yields a reduction of turbulent flame propagation speed, V_T, while pressure increase from 1 to 5 bar leads to an increase of V_T. On the other hand, both pressure and dilution contribute in decreasing the oscillations of the evaluated wrinkling factor, even though it must be taken into account that contour derives from Schlieren images.

Usually, it was observed a dependence of the flame propagation speed on the Reynolds and Karlovitz numbers. It was noticed that under the experimental conditions investigated on the spherical vessel, the increase of Ka leads to a slight reduction of V_T. On the contrary, increasing the Reynolds number enhance the resulting propagation speed. Other studies correlated similar evidences to the increase of

Ka and *Re* that reduces or increases, respectively, the flame surface wrinkling. In addition, the observed flame propagation speed enhancement due to the equivalence ratio increase is confirmed by other works as well.

NOSE LV configuration represents the experimental continuity between the two set-ups used in the present study. Anyway, it was showed that the sensibly lower integral length, for this configuration and, above all, for the two SV configurations, yields very low values of the Kolmogorov length scale. The direct consequence is an evident change in the flame structure that was confirmed by the flames images of the three configurations compared with those of the spherical vessel.

Firstly, it was found out that the points displacement on the Peters-Borghi diagram due to a pressure increase (up to 21 bar), follows the quadratic law of the laminar burning velocity decrease. This trend becomes evident only when pressure drastically increases with respect to the low-pressure range previously investigated (1-5 bar).

The comparison between tests performed on the two NOSE SV configurations shows that the effect of *Re* and *Ka* variations is similar to what is observed on the spherical vessel at lower pressure and higher integral length.

Last, recent correlations between turbulent flame propagation speed, laminar flame velocity and turbulent intensity proposed in literature were tested. As well, a new correlation was proposed and tested with the present experimental results and other data available in the current literature. It seems, that all data can follow the correlation: $\frac{S_T}{S_L} \propto a * Da * Ka^b$.

ACKNOWLEDGEMENTS

REFERENCES

[1]   R.G. Abdel-Gayed, K.J. Al-Kishali, D. Bradley, Turbulent burning velocities and flame

straining in explosions, Proc. R. Soc. London. A. Math. Phys. Sci. 391 (1801) (1984) 393–414

[2] D. Bradley, A.K.C. Lau, M. Lawes, Flame Stretch Rate as a Determinant of Turbulent Burning Velocity, Philos. Trans. R. Soc. London. Ser. A Phys. Eng. Sci. 338 (1650) (1992) 359–87

[3] J.F. Driscoll, Turbulent premixed combustion: Flamelet structure and its effect on turbulent burning velocities, Prog. Energy Combust. Sci. 34 (1) (2008) 91–134

[4] D. Bradley, M.Z. Haq, R.A. Hicks, T. Kitagawa, M. Lawes, C.G.W. Sheppard, et al., Turbulent burning velocity, burned gas distribution, and associated flame surface definition, Combust. Flame 133 (4) (2003) 415–30

[5] S. Daniele, P. Jansohn, J. Mantzaras, K. Boulouchos, Turbulent flame speed for syngas at gas turbine relevant conditions, Proc. Combust. Inst. 33 (2) (2011) 2937–44

[6] C.C. Liu, S.S. Shy, M.W. Peng, C.W. Chiu, Y.C. Dong, High-pressure burning velocities measurements for centrally-ignited premixed methane/air flames interacting with intense near-isotropic turbulence at constant Reynolds numbers, Combust. Flame (2012)

[7] S. Chaudhuri, F. Wu, D. Zhu, C.K. Law, Flame Speed and Self-Similar Propagation of Expanding Turbulent Premixed Flames, Phys. Rev. Lett. 108 (4) (2012) 44503

[8] F. Wu, A. Saha, S. Chaudhuri, C.K. Law, Propagation speeds of expanding turbulent flames of C4 to C8 n-alkanes at elevated pressures: Experimental determination, fuel similarity, and stretch-affected local extinction, Proc. Combust. Inst. 35 (2) (2015) 1501–8

[9] H. Kobayashi, K. Seyama, H. Hagiwara, Y. Ogami, Burning velocity correlation of methane/air turbulent premixed flames at high pressure and high temperature, Proc. Combust. Inst. 30 (1) (2005) 827–34

[10] H. Kobayashi, H. Hagiwara, H. Kaneko, Y. Ogami, Effects of CO2 dilution on turbulent premixed flames at high pressure and high temperature, Proc. Combust. Inst. 31 (1) (2007) 1451–8

[11] L.J. Jiang, S.S. Shy, W.Y. Li, H.M. Huang, M.T. Nguyen, High-temperature, high-pressure

burning velocities of expanding turbulent premixed flames and their comparison with Bunsen-type flames, Combust. Flame 172 (2016) 173–82

[12]   P. Ahmed, B. Thorne, M. Lawes, S. Hochgreb, G. V. Nivarti, R.S. Cant, Three dimensional measurements of surface areas and burning velocities of turbulent spherical flames, Combust. Flame 233 (2021) 111586

[13]   A.N. Lipatnikov, J. Chomiak, Effects of premixed flames on turbulence and turbulent scalar transport, Prog. Energy Combust. Sci. 36 (1) (2010) 1–102

[14]   P. Brequigny, F. Halter, C. Mounaïm-Rousselle, Lewis number and Markstein length effects on turbulent expanding flames in a spherical vessel, Exp. Therm. Fluid Sci. 73 (2016) 33–41

[15]   M. Lawes, M.P. Ormsby, C.G.W. Sheppard, R. Woolley, The turbulent burning velocity of iso-octane/air mixtures, Combust. Flame 159 (5) (2012) 1949–59

[16]   P. Brequigny, C. Endouard, F. Foucher, C. Mounaïm-Rousselle, Improvement of Turbulent Burning Velocity Measurements by Schlieren Technique, for High Pressure Isooctane-Air Premixed Flames, Combust. Sci. Technol. (2019) 1–17

[17]   O. Mannaa, P. Brequigny, C. Mounaim-Rousselle, F. Foucher, S.H. Chung, W.L. Roberts, Turbulent burning characteristics of FACE-C gasoline and TPRF blend associated with the same RON at elevated pressures, Exp. Therm. Fluid Sci. 95 (2018) 104–14

[18]   D. Bradley, M. Lawes, M.S. Mansour, Correlation of turbulent burning velocities of ethanol–air, measured in a fan-stirred bomb up to 1.2MPa, Combust. Flame 158 (1) (2011) 123–38

[19]   Q. Tang, H. Liu, M. Li, M. Yao, Z. Li, Study on ignition and flame development in gasoline partially premixed combustion using multiple optical diagnostics, Combust. Flame 177 (2017) 98–108

[20]   A.W. Skiba, T.M. Wabel, C.D. Carter, S.D. Hammack, J.E. Temme, J.F. Driscoll, Premixed flames subjected to extreme levels of turbulence part I: Flame structure and a new measured regime diagram, Combust. Flame 189 (2018) 407–32

[21]   Z.S. Li, B. Li, Z.W. Sun, X.S. Bai, M. Aldén, Turbulence and combustion interaction: High resolution local flame front structure visualization using simultaneous single-shot PLIF imaging of CH, OH, and CH2O in a piloted premixed jet flame, Combust. Flame (2010)

[22]   Z. Wang, B. Zhou, S. Yu, C. Brackmann, Z. Li, M. Richter, et al., Structure and burning velocity of turbulent premixed methane/air jet flames in thin-reaction zone and distributed reaction zone regimes, Proc. Combust. Inst. 37 (2) (2019) 2537–44

[23]   J.F. Driscoll, J.H. Chen, A.W. Skiba, C.D. Carter, E.R. Hawkes, H. Wang, Premixed flames subjected to extreme turbulence: Some questions and recent answers, Prog. Energy Combust. Sci. 76 (2020) 100802

[24]   N. Peters, The turbulent burning velocity for large-scale and small-scale turbulence, J. Fluid Mech. 384 (1999) 107–32

[25]   S.E. Trautwein, A. Grudno, G. Adomeit, The influence of turbulence intensity and laminar flame speed on turbulent flame propagation under engine like conditions, Symp. Combust. 23 (1) (1991) 723–8

[26]   M.T. Nguyen, D.W. Yu, S.S. Shy, General correlations of high pressure turbulent burning velocities with the consideration of Lewis number effect, Proc. Combust. Inst. 37 (2) (2019) 2391–8

[27]   E.M. Burke, F. Güthe, R.F.D. Monaghan, A Comparison of Turbulent Flame Speed Correlations for Hydrocarbon Fuels at Elevated Pressures, ASME Turbo Expo 2016: Turbomachinery Technical Conference and Exposition, Seoul, South KoreaIn, 2016, p. V04BT04A043

[28]   S.P.R. Muppala, N.K. Aluri, F. Dinkelacker, A. Leipertz, Development of an algebraic reaction rate closure for the numerical calculation of turbulent premixed methane, ethylene, and propane/air flames for pressures up to 1.0 MPa, Combust. Flame 140 (4) (2005) 257–66

[29]   M. Di Lorenzo, P. Brequigny, F. Foucher, C. Mounaïm-Rousselle, Validation of TRF-E as

gasoline surrogate through an experimental laminar burning speed investigation, Fuel 253 (2019) 1578–88

[30]   C. Mounaïm-Rousselle, L. Landry, F. Halter, F. Foucher, Experimental characteristics of turbulent premixed flame in a boosted Spark-Ignition engine, Proc. Combust. Inst. 34 (2) (2013) 2941–9

[31]   B. Galmiche, N. Mazellier, F. Halter, F. Foucher, Turbulence characterization of a high-pressure high-temperature fan-stirred combustion vessel using LDV, PIV and TR-PIV measurements, Exp. Fluids 55 (1) (2014) 1636

[32]   P. Brequigny, C. Endouard, C. Mounaïm-Rousselle, F. Foucher, An experimental study on turbulent premixed expanding flames using simultaneously Schlieren and tomography techniques, Exp. Therm. Fluid Sci. 95 (2018) 11–7

[33]   P. Brequigny, F. Halter, C. Mounaïm-Rousselle, T. Dubois, Fuel performances in Spark-Ignition (SI) engines: Impact of flame stretch, Combust. Flame 166 (2016) 98–112

[34]   C. Lhuillier, P. Brequigny, F. Contino, C. Mounaïm-Rousselle, Experimental investigation on ammonia combustion behavior in a spark-ignition engine by means of laminar and turbulent expanding flames, Proc. Combust. Inst. 38 (4) (2020) 5859–68

[35]   O. Nilaphai, C. Hespel, S. Chanchaona, C. Mounaïm-Rousselle, Spray and combustion characterizations of ABE/Dodecane blend in comparison to alcohol/Dodecane blends at high-pressure and high-temperature conditions, Fuel 225 (2018) 542–53

[36]   H. Ajrouche, O. Nilaphai, C. Hespel, F. Foucher, Impact of nitric oxide on n-heptane and n-dodecane autoignition in a new high-pressure and high-temperature chamber, Proc. Combust. Inst. 37 (3) (2019) 3319–26

[37]   O. Nilaphai, Vaporization and Combustion Processes of Alcohols and Acetone-Butanol-Ethanol (ABE) blended in n-Dodecane for High Pressure-High Temperature Conditions: Application to Compression Ignition Engine. PhD Thesis, Univ. Orléans, France, 2018,

[38] M. Di Lorenzo, P. Brequigny, F. Foucher, C. Mounaïm-Rousselle, New One Shot Engine Validation Based on Aerodynamic Characterization and Preliminary Combustion Tests, Flow, Turbul. Combust. (2020)

[39] D. Bradley, M. Lawes, M.S. Mansour, The problems of the turbulent burning velocity, Flow, Turbul. Combust. 87 (2–3) (2011) 191–204

[40] C. Meneveau, T. Poinsot, Stretching and quenching of flamelets in premixed turbulent combustion, Combust. Flame 86 (4) (1991) 311–32

[41] J.O. Hinze, Turbulence, McGraw-Hill, New York, 1975,

[42] J.F. Driscoll, Turbulent premixed combustion: Flamelet structure and its effect on turbulent burning velocities, Prog. Energy Combust. Sci. 34 (1) (2008) 91–134

[43] A.N. Lipatnikov, J. Chomiak, Turbulent flame speed and thickness: phenomenology, evaluation, and application in multi-dimensional simulations, Prog. Energy Combust. Sci. 28 (1) (2002) 1–74

[44] I. Han, K.Y. Huh, Roles of displacement speed on evolution of flame surface density for different turbulent intensities and Lewis numbers in turbulent premixed combustion, Combust. Flame 152 (1–2) (2008) 194–205

[45] S.A. Filatyev, J.F. Driscoll, C.D. Carter, J.M. Donbar, Measured properties of turbulent premixed flames for model assessment, including burning velocities, stretch rates, and surface densities, Combust. Flame 141 (1–2) (2005) 1–21

[46] T. Nilsson, H. Carlsson, R. Yu, X.S. Bai, Structures of turbulent premixed flames in the high Karlovitz number regime – DNS analysis, Fuel 216 (2018) 627–38

[47] Z. Wang, V. Magi, J. Abraham, Turbulent Flame Speed Dependencies in Lean Methane-Air Mixtures under Engine Relevant Conditions, Combust. Flame 180 (2017) 53–62

[48] S. Chaudhuri, F. Wu, C.K. Law, Scaling of turbulent flame speed for expanding flames with Markstein diffusion considerations, Phys. Rev. E 88 (3) (2013) 33005

[49] S. Wang, A.M. Elbaz, Z. Wang, W.L. Roberts, The effect of oxygen content on the turbulent flame speed of ammonia/oxygen/nitrogen expanding flames under elevated pressures, Combust. Flame 232 (2021) 111521

[50] A.J. Aspden, M.S. Day, J.B. Bell, Three-dimensional direct numerical simulation of turbulent lean premixed methane combustion with detailed kinetics, Combust. Flame 166 (2016) 266–83

[51] G. Nivarti, S. Cant, Direct Numerical Simulation of the bending effect in turbulent premixed flames, Proc. Combust. Inst. 36 (2) (2017) 1903–10

[52] S. Wang, A.M. Elbaz, Z. Wang, W.L. Roberts, The effect of oxygen content on the turbulent flame speed of ammonia/oxygen/nitrogen expanding flames under elevated pressures, Combust. Flame 232 (2021) 111521